Journal of The Electrochemical Society, **150** (8) A1052-A1059 (2003)
0013-4651/2003/150(8)/A1052/8/$7.00 © The Electrochemical Society, Inc.

In Situ Current Distribution Measurements in Polymer Electrolyte Fuel Cells

M. M. Mench,[a,*,z] C. Y. Wang,[a*] and M. Ishikawa[b]

[a]*Electrochemical Engine Center and Department of Mechanical and Nuclear Engineering, The Pennsylvania State University, University Park, Pennsylvania 16802, USA*
[b]*CD-adapco Japan, Limited, Yokohama, Japan*

There has been much recent interest and development of methods to accurately measure the current distribution in an operating polymer electrolyte fuel cell (PEFC). This paper presents results from a novel technique that uses a segmented flow field with standard, nonaltered membrane electrode assemblies and gas diffusion layers. Multiple current measurements are taken simultaneously with a multichannel potentiostat, providing high-resolution temporal and spatial distribution data. Current distribution data are shown that display the distributed effects of cathode stoichiometry variation and transient flooding on local current density. It is shown that the time scale for liquid accumulation in gas diffusion layer pores is much greater than that of any electrochemical or gas-phase species transport process. In order to facilitate state-of-the-art PEFC model validation, an idealized single-pass serpentine flow field was used, and the exact geometry is presented.
 [DOI: 10.1149/1.1584440]

Manuscript submitted September 9, 2002; revised manuscript received February 7, 2003. Available electronically June 16, 2003.

The hydrogen polymer electrolyte fuel cell (PEFC) has tremendous promise as a future power system due to its low pollution, high efficiency, and stealth. Many studies, too numerous to completely list, have examined various aspects of PEFC performance as a function of operating conditions.[1-10] Gottesfeld wrote an excellent review of PEFC components and operation, and the reader is referred to it for additional information on PEFC fundamentals.[11] In addition to experimental characterization, much research has focused on first-principles-based modeling of the PEFC.[12-23] However, advances in modeling have thus far outpaced the ability to experimentally verify the predicted performance. In particular, scant experimental data are presently available regarding current density and species distributions. As indicated by Wang,[24] it is this type of detailed validation that will permit an ultimate understanding of the physicochemical phenomena in PEFCs as well as development of computer-aided tools for design and development.

Determination of the current distribution is critical to understanding key phenomena including water management, CO poisoning, and reactant distribution effects. Weiser *et al.* described a novel technique utilizing a magnetic loop array embedded in the current collector plate to measure two-dimensional current distribution of a hydrogen PEFC.[25] The authors showed that cell compression can drastically affect local current density. Stumper *et al.* demonstrated three methods for the determination of current density distribution of a hydrogen PEFC.[26] First, the partial membrane electrode assembly (MEA) technique involves either masking different areas or partially catalyzing segments of the MEA to determine local current density behavior. Second, the subcell technique involves electrically isolating individual locations of catalyzed anode and opposing cathode from the main cell in order to measure the performance of the desired location. In the passive current mapping technique, an array of shunt resistors are located normal to an unmodified MEA surface, between the flowfield and a buss plate. Voltage sensors passively determine the potential drop across each resistor and, through Ohm's law, current distribution through the flow plate is determined. Cleghorn *et al.* implemented a printed circuit board approach for current density measurements using a segmented current collector, anode catalyst, and anode gas diffusion layer.[27]

While each of the described methods for determination of current distribution has advantages, it is desirable to utilize a nonsegmented MEA in order to preserve true fuel cell operation characteristics and avoid highly individualized specialty membranes. MEA segmentation is also undesirable because it does not simulate performance in a true fuel cell environment. In addition, predictive models are typically developed for a nonsegmented MEA.

In addition to use of conventional MEAs and good spatial resolution, the ability to determine transient effects from sudden changes in operating conditions is desired. The nonsegmented passive current mapping technique approach of Stumper *et al.*[26] allows transient measurement and has good spatial resolution but requires an array of embedded and highly precise shunt resistors. The magnetic loop method of Weiser *et al.* also allows transient measurements with unaltered MEAs and flowfields, but is more difficult to implement than the other methods, and cannot be applied to stacks.[25] Recently, Mench and Wang have demonstrated an improved technique for accurate current distribution measurements on direct methanol fuel cells that is applied to hydrogen PEFCs in this work.[28] Independently, Noponen *et al.* developed and demonstrated a similar technique.[29]

Experimental

Instrumented cell design.—In order to construct an electrically segregated flowfield, forty eight, 0.81 mm thick stainless steel current collecting ribs were gold-plated and embedded into an insulating polycarbonate slab with 0.89 mm wide gaps, as described by Finckh.[30] The ribs were arranged to produce a single-pass serpentine flowfield. Each rib was affixed to a gold-plated wire that extended through the polycarbonate for current collection. Figure 1 is a schematic diagram detailing the relevant dimensions of the fuel cell flow field. The diameter of the current-conducting wires that interface the gold-plated ribs with the data acquisition source was 0.81 mm. The dimension of the flow channel was chosen to be 2.16 mm wide, 3.18 mm deep, and had an average pass length of approximately 71 mm. With a total of 22 serpentine passes, the total path length was 1577 mm.

Teflon gaskets were press fit over the protruding gold-plated rib landings to form a flush surface with the polycarbonate slab. Two additional sealing gaskets were used to compensate for gas diffusion layer (GDL) thickness. Gold plating, and use of an optimized compression torque for the cell of 35 in-lbs, minimized electrical contact resistance between rib landings and the GDL. Pressure-indicating film (Pressurex by Sensor Products, Inc.) was used to determine the *in situ* pressure distribution of the landings onto the MEA as a function of compression torque. The assembly was checked to ensure a homogeneous pressure distribution from all landings onto the GDL, thus ensuring an even contact resistance distribution between the gold-plated landings and GDL. The area-specific contact resistance of this cell was found to be 41.7 $m\Omega\ cm^2$ using both four and two probe techniques, similarly to that described by Mench and Wang.[28]

* Electrochemical Society Active Member.
z E-mail: mmm124@psu.edu

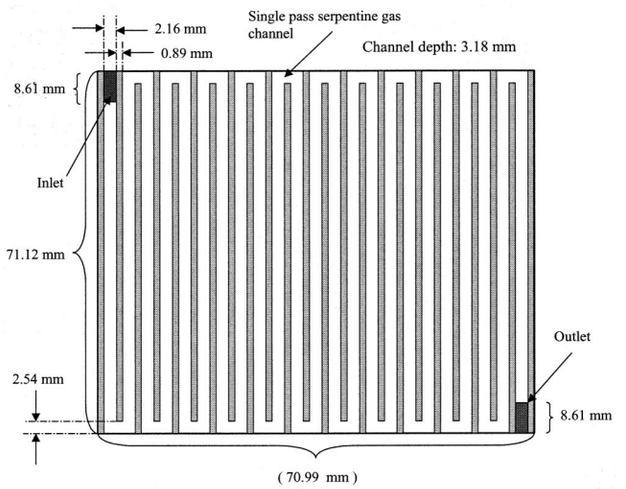

Figure 1. Schematic diagram of the 50 cm^2 instrumented test cell showing relevant dimensions.

The entire fuel cell assembly was leak proof tested to 0.3 MPa under water.

A schematic of the test and control system is shown in Fig. 2. Ultrahigh-purity (>99.999%) hydrogen and standard compressed air were supplied from gas cylinders. A steam-injection humidifier system (Lynntech, Inc.) was used to provide desired humidification to anode and cathode flows through control of the precise amount of water vapor added to the gas streams. Between humidifier and fuel cell, electric heating tapes were used to eliminate any condensation. Directly upstream of the inlet to the fuel cell, a gas sampling port was installed to directly measure the input humidity to the fuel cell by an Agilent 3000 MicroGC with PlotU column. This provided accurate measurement and control of the humidification entering the cell.

The fuel cell system, including all lines leading to the fuel cell, was heated to the desired temperature, which was maintained with several Omega Engineering, Inc., model 8500 PID controllers. The cell and input lines maintained a steady temperature after suitable time to eliminate thermal transients. This start-up time was determined to be about 90 min by system validation tests using thermocouples affixed to the GDL under nonflowing conditions.

To control and measure accurate current/voltage polarization curves, the fuel cell was connected to a multichannel potentiostat/galvanostat (Arbin Instruments). The active current density mapping method used in this paper is fundamentally similar and is essentially a modification of the passive current density mapping technique of Stumper *et al.*[26] However, an electrically segmented flowfield/current collector replaces the separate array of shunt resistors normal to the MEA. The segmented flowfield is in direct contact with the unaltered GDL on the anode and cathode. This technique eliminates the challenge to reduce current spreading due to high in-plane conductivity of the flowfield plates. Instead, a gold-plated, electrically segmented current collector is used and repeatable current density data can be obtained. In this active current density mapping technique, the potentiostat system maintains a constant voltage and the current sensors measure amperage emerging from each segmented current collector location, without the need for shunt resistors.

It is important to note that this technique measures the current density distribution of an operating cell as it flows from the GDL into the current collection plate, not as it emerges from the catalyst layer. Although current spreading through the GDL occurs, this is similar to a real operating system. Artificially segmenting the MEA disrupts the current distribution reaching the current collectors and is therefore inappropriate for these measurements or model validation. Even with GDL segmentation, one will not measure current density in the catalyst layer only. With either a segmented or nonsegmented approach, one measures the current density as a result of ionic resistance distribution in the electrolyte, as well as the catalyst layer. The approach used measures the current coming out of a fuel cell GDL, as in a real stack. Cross talk between two channels is expected, as happens in a real fuel cell situation, but it is limited by a relatively large in-plane resistance of the GDL/catalyst layer parallel circuit, compared to the very low through-plane GDL resistance.

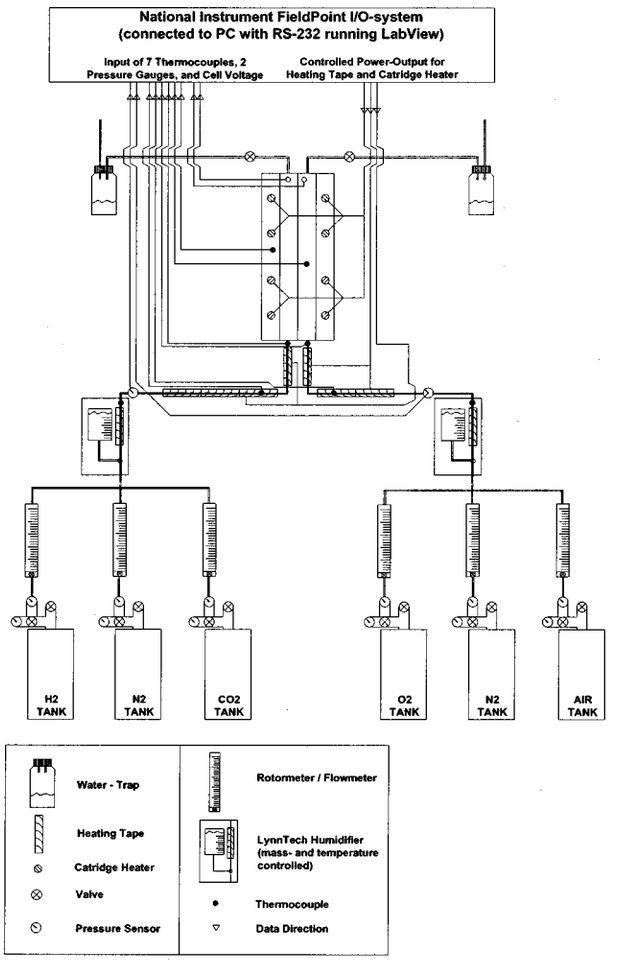

Figure 2. Schematic of the experimental test stand and control system.

Calculation of active area segments.—To calculate the current density of a set of current collecting landings, the active areas directly under the landings and half the adjacent gas channels were taken. The reported measurement location along the cathode flow path is the center of this total area in the flow path. Area under current collection landings is counted toward current density calculations. It is important to note that the data are represented as current density at a discrete distance along the flowpath, when it actually is integrated over a distributed region. In order to represent this area as a discrete location, the relative lengths have been weighted in order to take adjacent channels into account and more accurately represent the mean location of current collection. This discretization gave very consistent results.

The membrane electrode assemblies (MEAs) used consisted of Nafion 112 as the polymeric membrane sandwiched between the catalyst and ELAT carbon cloth diffusion layers. All MEAs used had a catalyst loading of 0.5 mg Pt/cm^2 on both anode and cathode. Other general operating conditions are given in Table I.

Table I. Baseline operating conditions.

Parameter	Value	Units
Electrolyte	Nafion 112	NA
GDL	ELAT (De Nora North America) anode and cathode	NA
Catalyst loading (carbon supported)	0.5	mg/cm^2
Cell temperature	80	°C
Anode inlet temperature	90	°C
Cathode inlet temperature	80	°C
Anode and cathode pressure	0.1-0.2	MPa
Anode humidification	100% at 90°C	NA
Cathode humidification	100% at 80°C	NA
Anode gas	Ultrahigh-purity H_2 (>99.999%)	NA
Cathode gas	Commercial air (79% N_2, 21% O_2)	NA

Results and Discussion

Homogeneous distribution.—It is expected that at relatively high mass flow rates with full humidification and low pressures, a nearly uniform distribution of current would result. An experiment was designed to observe this condition. The distributed polarization curve for this experiment is shown in Fig. 3. There is some indication of flooding, as can be seen from the characteristic ''comma''-shaped[26,28] local polarization curve for the channels closest to the cathode exit location. The two channels near the end of the cathode path, at $x/L = 0.891$ and 0.964 (corresponding to 89 and 96% along the length of the single serpentine cathode path), roll over into comma shapes at low cell voltage, while the overall bulk cell output increases. The current density *vs.* fractional location along the cathode flow path at several cell voltages is given in Fig. 4. From Fig. 4, a nearly homogeneous current distribution can be seen, except at very low cell voltage (0.4 V) corresponding to high current output and near depletion of hydrogen in the anode. The comma-shaped curve, observed in other studies,[26,28] is a result of mass-transport limitations and can indicate local flooding or reactant depletion, as discussed in the following sections.

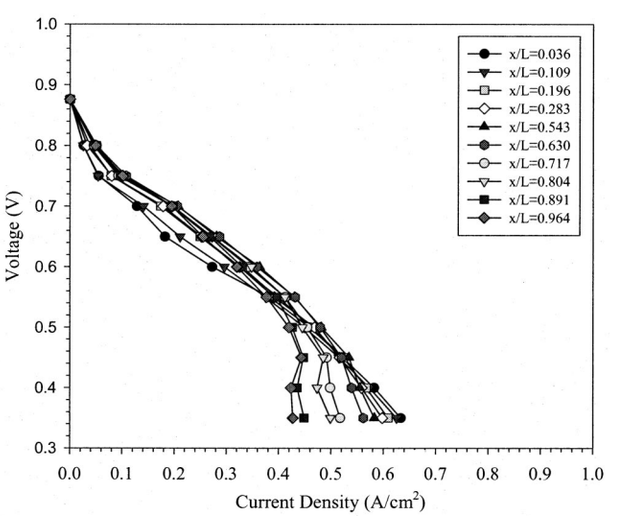

Figure 3. Steady-state distributed polarization curve for a low-pressure, fully humidified, high-flow-rate condition. Cell temperature 80°C; anode inlet humidity 100% RH at the rate of 90°C; cathode inlet humidity 100% RH at the rate of 80°C; $\xi_a = 0.7$ A/cm^2 equiv; $\xi_c = 1.75$ A/cm^2 equiv; anode and cathode exit pressure 1 atm.

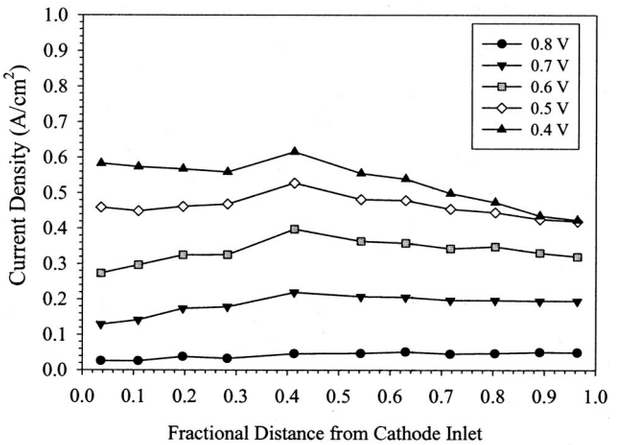

Figure 4. Performance *vs.* fractional location along the cathode path for a fully humidified, high flow rate condition. Cell temperature 80°C; anode inlet humidity 100% RH at the rate of 90°C; cathode inlet humidity 100% RH at the rate of 80°C; $\xi_a = 0.7$ A/cm^2 equiv; $\xi_c = 1.75$ A/cm^2 equiv; and anode and cathode exit pressure 1 atm.

The effect of cathode stoichiometry.—In PEFCs, the performance is extremely sensitive to cathode stoichiometry due to relatively sluggish oxygen reduction kinetics and mass transport. In order to isolate the effects of stoichiometry from accumulated flooding, a rapid-scan polarization curve was taken to prevent sufficient time for flooding to occur and affect measured performance. For the rapid scan, the applied voltage was varied at a rate of 5-10 mV/s in increments of 50 mV. This provided very reproducible data with generally higher performance than steady-state values, in which 30 min to an hour elapses between voltage variations at low cell voltage, to allow time for flooding accumulation to reach steady state.

The rapid-scan technique is designed to separate, as much as possible, the two-phase flooding effects from the gas-phase mass-transport and electrochemical effects. Since the time required for performance degradation due to liquid accumulation is relatively slow (on the order of minutes, shown later in this paper) compared to gas-phase transport time constants (on the order of 0.1-1 s) and the electrochemical capacitance time constant, this technique leaves little time for flooding accumulation to occur. The gas-phase time constant for mass distribution adjustment in the GDL can be estimated as

$$\tau_{\text{gas phase}} = \frac{\delta_{\text{GDL}}^2}{D_{\text{gas}}^{\text{eff}}} \cong \text{O}(0.1 - 1 \text{ s}) \qquad [1]$$

where δ_{GDL} is the GDL thickness and $D_{\text{gas}}^{\text{eff}}$ is the effective diffusivity of gas, modified for the porous nature of the GDL. Use of typical values of porosity GDL thickness and diffusivity along with a Bruggeman correlation for effective diffusivity leads to the predicted time scale. The rapid-scan technique is like a bandpass filter, in that it will not completely eliminate unwanted two-phase effects from occurring, but they are greatly reduced. The results of the rapid scan are therefore appropriate for model validation in the absence of two-phase effects.

A high anode stoichiometry of 1.875 A/cm^2 equiv (*i.e.*, stoichiometry would be 1.0 at $i = 1.875$ A/cm^2) was used for this series of tests so that no appreciable mass-transport limitation on the anode exists. Cell humidification was full at 90 and 80°C on the anode and cathode, respectively. Cell temperature was maintained at 80°C and cell inlet pressure was maintained at 1.5 atm. Cathode stoichiometry was varied from 1.125 to 2.25 A/cm^2 equiv. It is important to note that the flow rate is constant for each test run. That is, the flow rate was not varied as a function of current density.

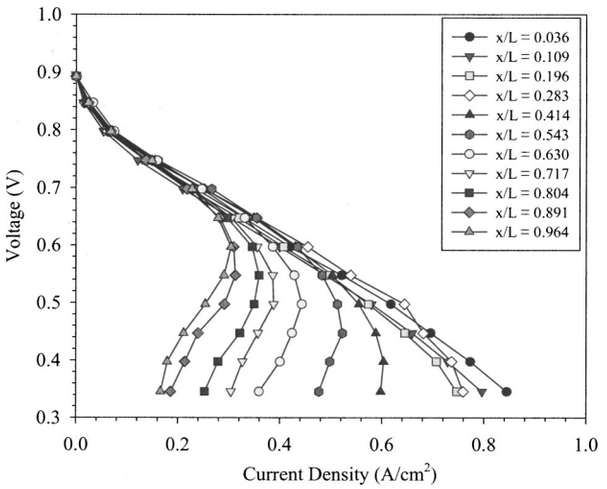

Figure 5. Distributed rapid-scan polarization curve for low cathode stoichiometry of 1.125 A/cm^2 equiv showing mass-transport-limited performance. Cell temperature 80°C; anode inlet humidity 100% RH at the rate of 90°C; cathode inlet humidity 100% RH at the rate of 80°C; ξ_a = 1.875 A/cm^2 equiv; and anode and cathode exit pressure 1.5 atm.

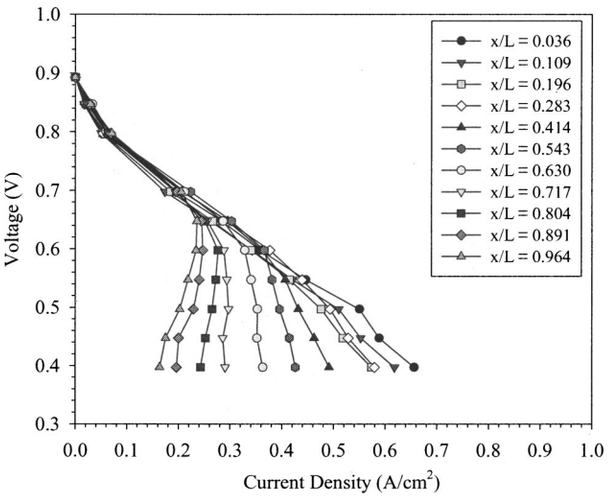

Figure 7. Distributed steady-state polarization curve for low cathode stoichiometry of 1.125 A/cm^2 equiv, showing mass-transport-limited performance. Cell temperature 80°C; anode inlet humidity 100% RH at the rate of 90°C; cathode inlet humidity 100% RH at the rate of 80°C; ξ_a = 1.875 A/cm^2 equiv; and anode and cathode exit pressure 1.5 atm.

Low cathode stoichiometry of 1.125 A/cm^2 equiv.—Figures 5 and 6 are plots of the distributed polarization curves and current density *vs.* fractional location along the cathode flow path for the case of low cathode stoichiometry. From Fig. 5 it can be seen that severe mass-transport limitations exist at low cell voltage. The comma-shaped curves resemble the characteristic shape of flooded distributions from Mench and Wang.[28] As discussed, the polarization curves were taken with a high enough voltage scan rate to avoid significant flooding accumulation. Therefore, the performance limitation can be attributed to mass-transport losses at the cathode, and the comma-shaped curve is a characteristic feature of a fuel cell operating in a mass-limiting condition, whether from flooding or low stoichiometry. The distribution of performance along the cathode channel shown in Fig. 6 is in agreement with this conclusion, as performance decreases monotonically with distance along the cathode channel for high current densities. For low values of current density, a nearly homogeneous distribution is observed, corresponding to the abundant supply of oxygen for these low-power conditions.

As discussed, the data in Fig. 5 and 6 were taken with a rapid-scan technique. Figures 7 and 8 are a distributed polarization curve and a performance variation *vs.* location plot, deduced from data taken allowing adequate time for steady state. That is, these figures show the steady-state values for the performance at identical conditions of Fig. 5, except about an hour elapsed between each cell voltage increment below 0.6 V. It can be seen that the steady-state curves all suffer reduced performance compared to the corresponding results taken with the rapid scan, especially for lower cell voltage corresponding to larger current density (and hence cathodic water production). This reduced performance is attributable to the pore

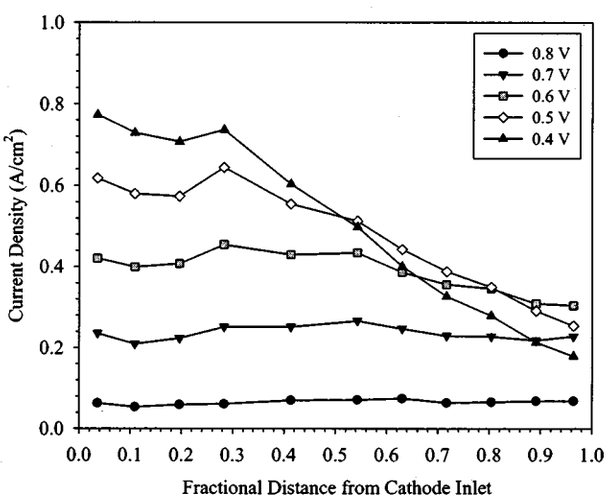

Figure 6. Rapid-scan performance *vs.* fractional location for low cathode stoichiometry of 1.125 A/cm^2 equiv, showing mass-transport-limited performance at high current density. Cell temperature 80°C; anode inlet humidity 100% RH at the rate of 90°C; cathode inlet humidity 100% RH at the rate of 80°C; ξ_a = 1.875 A/cm^2 equiv; and anode and cathode exit pressure 1.5 atm.

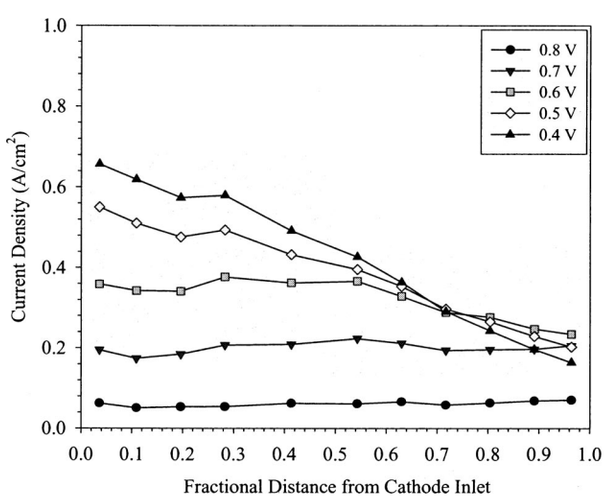

Figure 8. Steady-state performance *vs.* fractional location for low cathode stoichiometry of 1.125 A/cm^2 equiv, showing mass-transport-limited performance at high current density. Cell temperature 80°C; anode inlet humidity 100% RH at the rate of 90°C; cathode inlet humidity 100% RH at the rate of 80°C; ξ_a = 1.875 A/cm^2 equiv; and anode and cathode exit pressure 1.5 atm.

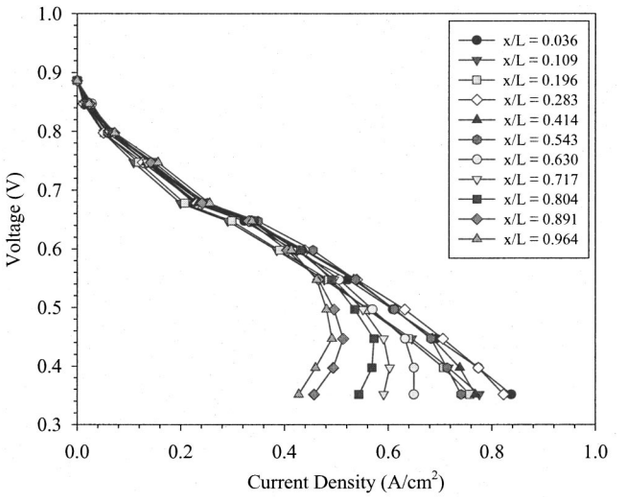

Figure 9. Rapid-scan distributed polarization curve at a cathode stoichiometry of 1.5 A/cm^2 equiv, showing reduced mass-transport-limited performance. Cell temperature 80°C; anode inlet humidity 100% RH at the rate of 90°C; cathode inlet humidity 100% RH at the rate of 80°C; ξ_a = 1.875 A/cm^2 equiv; and anode and cathode exit pressure 1.5 atm.

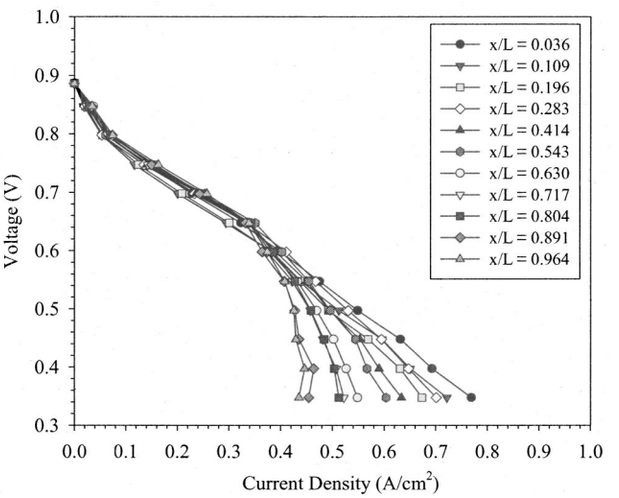

Figure 11. Distributed steady-state polarization curve at a cathode stoichiometry of 1.5 A/cm^2 equiv, showing mass-transport-limited performance. Cell temperature 80°C, anode inlet humidity 100% RH at the rate of 90°C; cathode inlet humidity 100% RH at the rate of 80°C; ξ_a = 1.875 A/cm^2 equiv; and anode and cathode exit pressure 1.5 atm.

blockage effect of liquid accumulation in the GDL resulting from cathode flooding at high current densities.

Increased cathode stoichiometry of 1.50 A/cm^2 equiv.—As the cathode stoichiometry and flow rate of air is increased, it is expected that the severe performance limitations observed in Fig. 5 would be somewhat diminished. This is observed, as can be seen in Fig. 9-12, which are polarization and current density distribution plots for a cathode stoichiometry of 1.50 A/cm^2 equiv for both rapid-scan and steady-state measurements. Although the performance is improved compared to the case of 1.125 A/cm^2 equiv cathode stoichiometry, significant mass-transport limitations still exist at high current densities. In comparison of Fig. 5 to Fig. 9, the bulk fuel cell performance is increased and the location and severity of the decrease in output has been pushed further downstream in the cathode flow channel. The point at which the distributed polarization curve rolls over into a mass-limited comma shape has been pushed from ~40% downstream to ~60% downstream. Once again, the steady-state curves all suffer reduced performance compared to the corresponding results taken with the rapid scan, especially at lower cell voltages corresponding to larger mean current density.

Increased cathode stoichiometry of 1.875 A/cm^2 equiv.—Figures 13 and 14 are a rapid-scan distributed polarization plot and a current density *vs.* location plot for a cathode stoichiometry of 1.875 A/cm^2 equiv. This condition is expected to exhibit decreased mass-transport limitation on the cathode compared to lower cathode stoichiometry. From Fig. 13 it is seen that the distributed polarization curves are closer together, indicating a more homogeneous overall distribution compared to lower stoichiometry conditions. Also, the bulk fuel cell performance is increased, and the location and severity of the de-

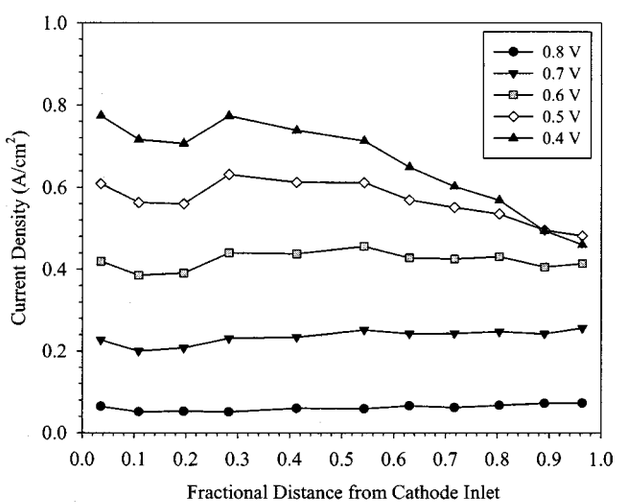

Figure 10. Rapid-scan performance *vs.* fractional location at a cathode stoichiometry of 1.5 A/cm^2 equiv, showing mass-transport-limited performance at high current density. Cell temperature 80°C; anode inlet humidity 100% RH at the rate of 90°C; cathode inlet humidity 100% RH at the rate of 80°C; ξ_a = 1.875 A/cm^2 equiv; anode and cathode exit pressure 1.5 atm.

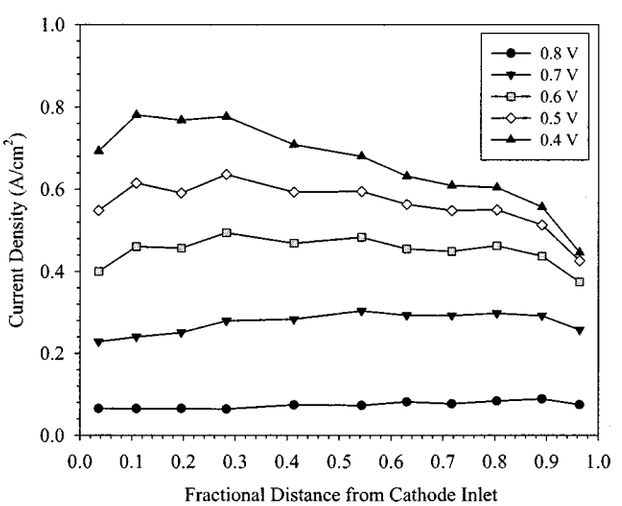

Figure 12. Steady-state performance *vs.* fractional location at a cathode stoichiometry of 1.5 A/cm^2 equiv, showing mass-transport-limited performance at high current density. Cell temperature 80°C, anode inlet humidity 100% RH at the rate of 90°C; cathode inlet humidity 100% RH at the rate of 80°C; ξ_a = 1.875 A/cm^2 equiv; anode and cathode exit pressure 1.5 atm.

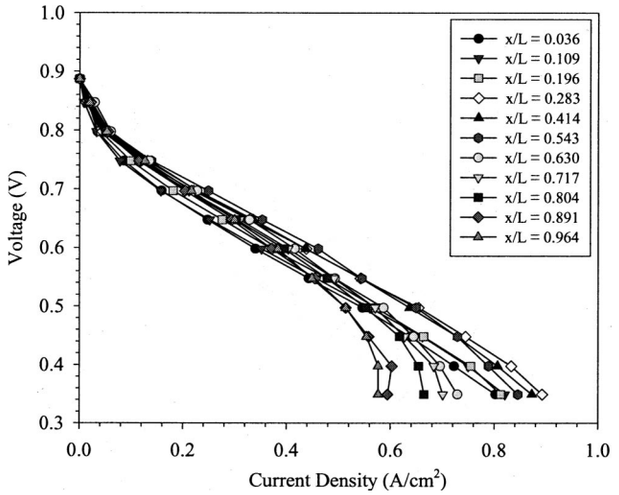

Figure 13. Distributed rapid-scan polarization curve for a cathode stoichiometry of 1.875 A/cm^2 equiv. Cell temperature 80°C, anode inlet humidity 100% RH at the rate of 90°C, cathode inlet humidity 100% RH at the rate of 80°C, ξ_a = 1.875 A/cm^2 equiv; and anode and cathode exit pressure 1.5 atm.

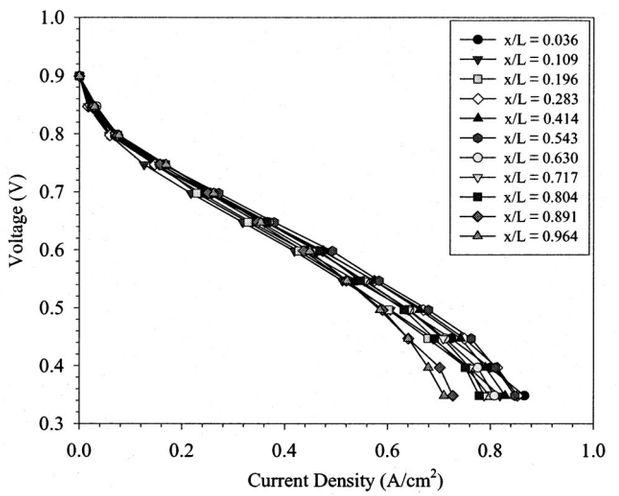

Figure 15. Distributed rapid-scan polarization curve for a cathode stoichiometry of 2.25 A/cm^2 equiv. Cell temperature 80°C; anode inlet humidity 100% RH at the rate of 90°C; cathode inlet humidity 100% RH at the rate of 80°C; ξ_a = 1.875 A/cm^2 equiv; and anode and cathode exit pressure 1.5 atm.

crease in output due to mass transport has been pushed farther downstream in the cathode flow channel. The location at which the distributed polarization curve rolls over into a comma shape has been pushed from ~60% for the ξ_c = 1.5 case to ~80% downstream for this case. It is seen, then, that even at this high cathode stoichiometry there is still some portion of the fuel cell that is not performing to full potential due to cathode reactant deficiency.

It can be seen from Fig. 12 and 14 that the inlet portion of the fuel cell flow path has a reduced performance that is a function of current density. The difference in active area is accounted for in the calculation for edge location current densities. This phenomenon may be attributed to some anode-side membrane drying at the inlet caused by electro-osmotic drag (this would be lessened downstream by accumulation of water on the cathode and enhanced back-diffusion, and does appear to be a function of the current density from Fig. 12 and 14). However, there are perhaps other effects, such as imperfect catalyst layer spread on the MEA (*e.g.*, catalyst layer is not a perfect square), nonisothermal effects, or other experimental error that may cause this slight deviation.

Increased cathode stoichiometry of 2.25 A/cm^2 equiv.—Figures 15 and 16 show a rapid-scan distributed polarization curve and a current density *vs.* location curve for a cathode stoichiometry of 2.25 A/cm^2 equiv. From Fig. 15 it is seen that the distributed polarization curves are much closer together, indicating a more homogeneous overall distribution compared to lower stoichiometry cases. There does not appear to be any location within the cathode that suffers severe performance loss due to oxidizer mass limitation at any current density tested. Each increase in cathode stoichiometry of 0.375 A/cm^2 equiv pushed the location of performance rollover

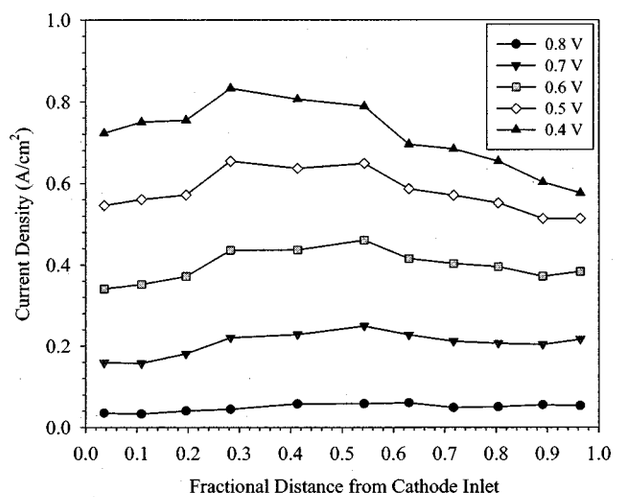

Figure 14. Rapid-scan performance *vs.* fractional location for a cathode stoichiometry of 1.875 A/cm^2 equiv. Cell temperature 80°C; anode inlet humidity 100% RH at the rate of 90°C; cathode inlet humidity 100% RH at the rate of 80°C, ξ_a = 1.875 A/cm^2 equiv; and anode and cathode exit pressure 1.5 atm.

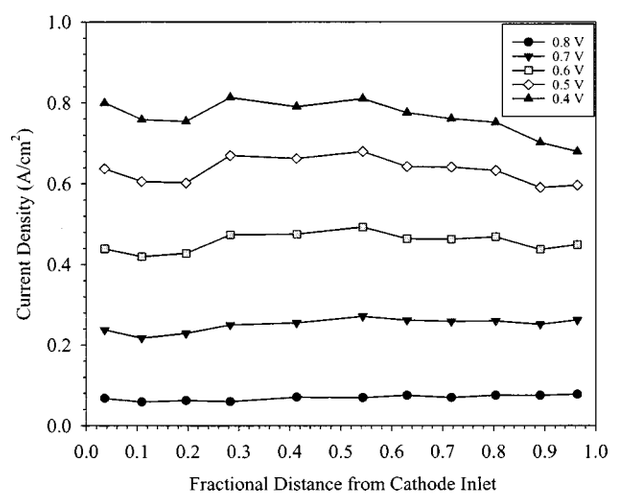

Figure 16. Rapid-scan performance *vs.* fractional location for a cathode stoichiometry of 2.25 A/cm^2 equiv. Cell temperature 80°C; anode inlet humidity 100% RH at the rate of 90°C; cathode inlet humidity 100% RH at the rate of 80°C; ξ_a = 1.875 A/cm^2 equiv; and anode and cathode exit pressure 1.5 atm.

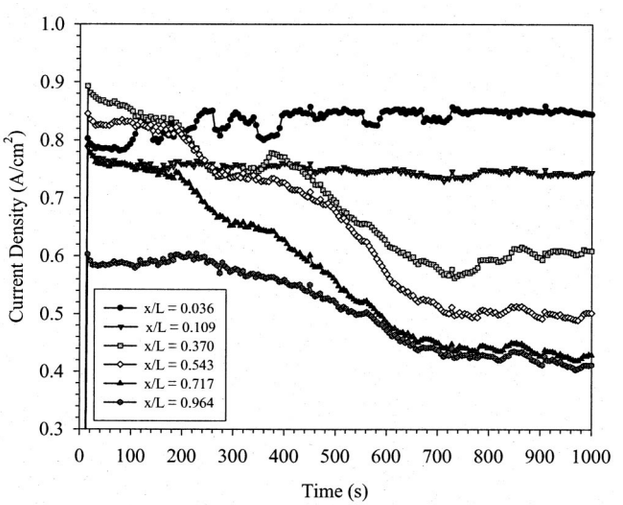

Figure 17. Distributed performance data after perturbation from V_{cell} = 0.55 to 0.5 V. Slow flooding accumulation is seen to degrade performance over nearly 20 min. Transient performance cell temperature 80°C; anode inlet humidity 100% RH at the rate of 90°C; cathode inlet humidity 100% RH at the rate of 80°C; ξ_a = 1.5 A/cm^2 equiv, ξ_c = 2.5 A/cm^2 equiv, anode and cathode exit pressure 2 atm.

downstream 20%, beginning with a rollover location of ~40% at ξ_c = 1.125. This is not a universal result and is a function of cell design and total performance at a given voltage.

Discussion on flooding and definition of steady state.—It is appropriate to discuss the definition of steady state used. This is because in a vast majority of PEFC publications, the definition is ambiguous. The majority of published work reports polarization data based on rapid-scan polarization curves, similar to those presented in this work where noted. While these data are highly useful for separation of the effects of flooding from stoichiometry mass-transport limitations or humidity variation, they do not necessarily represent the true steady state that would be achieved if the given cell condition was held indefinitely.

At high current densities, it is possible to have a flooded cathode and dry anode, due to electro-osmotic drag depletion. However, for very thin membranes such as Nafion 112 (51 μm), back-diffusion of water from the cathode to anode can compensate for the drag.[31] It follows for a fuel cell operated at full humidification on the cathode and anode sides, that any creation of water will generate some liquid water accumulate, blocking GDL pores and inducing flooding, assuming isothermal conditions, which will not be the case at high current density conditions. In addition, as the operating pressure is increased in the fuel cell, the volume flow rate and hence velocity of the gas is reduced proportionally with absolute pressure. This reduced flow rate has the effect of reducing mass transfer between the channels and the MEA and tends to limit water accumulation in the gas flow to the theoretical thermodynamic limit by reducing droplet entrainment. It is expected that at high-pressure operating conditions and full humidification, significant cathode flooding should occur because flow enters the anode and cathode at super and fully saturated conditions, respectively, and water is generated by oxygen reduction reaction at the cathode.

Where flooding occurs, the location of flooding shows a gradual decrease in performance corresponding to the gradual accumulation of liquid water. This process can take minutes to hours, depending on the initial condition of the MEA. Figure 17 shows flooding degradation for a sudden cell voltage perturbation from 0.55 to 0.50 V. Immediately following perturbation, the current density generally adjusts to a high value corresponding to the increased overpotential to drive the electrochemical reactions. The performance then degrades to a steady-state value. More interestingly, it is seen that the local current densities near the cathode inlet (*i.e.*, x/L = 0.036 and 0.109) jump to high values and remain there due to the absence of pore flooding. In the middle section of the fuel cell (*i.e.*, x/L = 0.370 and 0.543), the local current densities undergo substantial decay after the initial jump in performance due to liquid accumulation in pores and more moist air coming from upstream. Near the cathode exit, the local current densities respond little to the initial voltage perturbation due to depleted reactant, and then experience a decay due to flooding.

It has been observed that, depending on the initial state, there can be multiple steady states, depending on the history of operation. This is a result of the relatively long time scales of GDL pore filling and recovery compared to electrochemical and gas-transport processes. As an example, once the flooding condition has been allowed to fully accumulate and reach steady state, a sudden decrease in cell voltage does not induce much change in output. However, the same voltage perturbation occurring from a nonflooded initial condition induces a sharp initial change, followed by a gradual flooding process to nearly the same final ''fully flooded'' state. Therefore, transient flooding data are highly dependent on initial conditions. A thorough treatment of these transient flooding effects is beyond the scope of this paper.

Conclusions

A robust current mapping technique based on segmented flow field and a multichannel potentiostat was successfully implemented to study H_2 PEFCs. Along with other diagnostic techniques such as water distribution mapping,[32] this current mapping technique provides an important tool to understand water management and reactant distribution in PEFCs. While simple to implement and convenient to measure, this technique has been demonstrated to provide spatial and temporal current distribution data with high resolution. Specifically:

1. Benchmark current and species distribution data have been obtained using a specially designed single-pass serpentine fuel cell. These data are particularly valuable for computational fuel cell dynamics (CFCD) model validation.

2. Data were presented that systematically show the effect of cathode flow rate. The location within the cathode flow channel of mass-limited performance was shown to be a function of cathode stoichiometry.

3. The time scale of cathode flooding was shown to be quite slow relative to other transport and electrochemical phenomena. Transient current density results demonstrate a slow flooding process that does not reach a steady state for several minutes of operation. Recovery is similarly slow.

Acknowledgments

Financial support of CD-Adapco Japan is gratefully acknowledged. Additionally, C.Y.W. acknowledges partial support of the U.S. Department of Energy and Conoco under cooperative agreement no. DEFC26-01NT41098. The authors also acknowledge the contributions of Oliver Finckh and Qunlong Dong in the design of the fuel cell and calibration of the test stand components.

The Pennsylvania State University assisted in meeting the publication costs of this article.

References

1. D. M. Bernardi, *J. Electrochem. Soc.*, **137**, 3344 (1990).
2. A. Parthasarathy, S. Srinivasan, A. J. Appleby, and C. Martin, *J. Electrochem. Soc.*, **139**, 2856 (1992).
3. A. Parthasarathy, S. Srinivasan, A. J. Appleby, and C. Martin, *J. Electrochem. Soc.*, **139**, 2530 (1992).
4. Y. W. Rho, O. A. Velev, S. Srinivasan, and Y. T. Kho, *J. Electrochem. Soc.*, **141**, 3838 (1994).
5. J. C. Amphlett, R. M. Baumert, R. F. Mann, B. A. Peppley, P. R. Roberge, and T. J. Harris, *J. Electrochem. Soc.*, **142**, 9 (1995).
6. R. Mosdale and S. Srinivasan, *Electrochim. Acta*, **40**, 413 (1995).
7. H.-F. Oetjen, V. M. Schmidt, U. Stimming, and F. Trila, *J. Electrochem. Soc.*, **143**, 3838 (1996).

8. F. N. Büchi and D. Srinivasan, *J. Electrochem. Soc.*, **144**, 2767 (1997).
9. F. A. Uribe, S. Gottesfeld, and T. A. Zawodzinski, *J. Electrochem. Soc.*, **149**, A293 (2002).
10. E. A. Ticianelli, C. R. Derouin, and S. Srinivasan, *J. Electroanal. Chem. Interfacial Electrochem.*, **251**, 275 (1988).
11. S. Gottesfeld, in *Advances in Electrochemical Science and Engineering*, C. Tobias, Editor, Vol. 5, Wiley and Sons, New York (1997).
12. T. E. Springer, T. A. Zawodzinski, and S. Gottesfeld, *J. Electrochem. Soc.*, **138**, 2334 (1991).
13. D. M. Bernardi and M. W. Verbrugge, *AIChE J.*, **37**, 1151 (1991).
14. D. M. Bernardi and M. W. Verbrugge, *J. Electrochem. Soc.*, **139**, 2477 (1992).
15. T. E. Springer, M. S. Wilson, and S. Gottesfeld, *J. Electrochem. Soc.*, **140**, 3513 (1993).
16. T. F. Fuller and J. Newman, *J. Electrochem. Soc.*, **140**, 1218 (1993).
17. T. V. Nguyen and R. E. White, *J. Electrochem. Soc.*, **140**, 2178 (1993).
18. C. Y. Wang and W. B. Gu, *J. Electrochem. Soc.*, **145**, 3418 (1998).
19. V. Gurau, H. Liu, and S. Kakac, *AIChE J.*, **44**, 2410 (1998).
20. J. S. Yi and T. V. Nguyen, *J. Electrochem. Soc.*, **146**, 38 (1999).
21. S. Um, C. Y. Wang, and K. S. Chen, *J. Electrochem. Soc.*, **147**, 4485 (2000).
22. Z. H. Wang, C. Y. Wang, and K. S. Chen, *J. Power Sources*, **94**, 40 (2001).
23. C. Y. Wang, S. Um, H. Meng, U. Pasaogullari, and Y. Wang, in *2002 Fuel Cell Seminar* (Nov 2002).
24. C. Y. Wang, in *Handbook of Fuel Cells*, W. Vielstich, Editor, Vol. 3, Chap. 29, p. 337, John Wiley & Sons, New York (2003).
25. C. Wieser, A. Helmbold, and E. Gülzow, *J. Appl. Electrochem.*, **30**, 803 (2000).
26. J. Stumper, S. Campell, D. Wilkinson, M. Johnson, and M. Davis, *Electrochim. Acta*, **43**, 3773 (1998).
27. S. Cleghorn, C. Derouin, M. Wilson, and S. Gottesfeld, *J. Appl. Electrochem.*, **28**, 663 (1998).
28. M. Mench and C. Y. Wang, *J. Electrochem. Soc.*, **150**, A79 (2003).
29. M. Noponen, T. Mennola, M. Mikkola, T. Hottinen, and P. Lund, *J. Power Sources*, **106**, 304 (2002).
30. O. H. Finckh, M.S. Thesis, The Pennsylvania State University, University Park, PA (2002).
31. G. J. Janssen, *J. Electrochem. Soc.*, **148**, A1313 (2001).
32. O. H. Finckh, M. M. Mench, Q. Dong, and C. Y. Wang, in *2002 Fuel Cell Seminar* (Nov 2002).